Helical modes generate antimagnetic rotational spectra in nuclei

Sham S. Malik*
Department of Physics, Guru Nanak Dev University, Amritsar-143005, India

(Received 16 October 2017; revised manuscript received 5 January 2018; published 27 March 2018)

A systematic analysis of the antimagnetic rotation band using r-helicity formalism is carried out for the first time. The observed octupole correlation in a nucleus is likely to play a role in establishing the antimagnetic spectrum. Such octupole correlations are explained within the helical orbits. In a rotating field, two identical fermions (generally protons) with paired spins generate these helical orbits in such a way that its positive (i.e., up) spin along the axis of quantization refers to one helicity (right-handedness) while negative (down) spin along the same quantization-axis decides another helicity (left-handedness). Since the helicity remains invariant under rotation, therefore, the quantum state of a fermion is represented by definite angular momentum and helicity. These helicity represented states support a pear-shaped structure of a rotating system having z axis as the symmetry axis. A combined operation of parity, time-reversal, and signature symmetries ensures an absence of one of the signature partner band from the observed antimagnetic spectrum. This formalism has also been tested for the recently observed negative parity $\Delta I = 2$ antimagnetic spectrum in odd-A ^{101}Pd nucleus and explains nicely its energy spectrum as well as the $B(E2)$ values. Further, this formalism is found to be fully consistent with twin-shears mechanism popularly known for such type of rotational bands. It also provides significant clue for extending these experiments in various mass regions spread over the nuclear chart.

DOI: 10.1103/PhysRevC.97.034325

I. INTRODUCTION

In nearly spherical nuclei, regular rotation-like bands indicate the unusual type of collectivity, wherein a few high-j valence particle and hole states become available for correlated alignment. At the bandhead, due to the shape of their density distribution, the valence particle (hole) angular-momentum vector aligns itself towards the nuclear symmetry axis, whereas the hole (particle) angular momentum aligns itself towards an axis perpendicular to it. The resultant angular momentum lies somewhere between the two. Along the band, the angular momentum increases due to a gradual alignment of the particle and hole angular momenta into the direction of the resultant angular momentum. This coupling appears like a closing of a pair of shears, and hence the term shears mechanism [1–3] was assigned to this type of excitation. In this mechanism, the magnetic dipole moment vector arises mainly from proton particles (holes) and neutrons holes (particles) by rotating around the resultant angular-momentum vector and acts as an oder parameter inducing a violation of rotational symmetry. This forms an analogy to a ferromagnet, where the total magnetic dipole moment (equal to sum of the atomic magnetic dipole moments) is an order parameter.

Parallel to ferromagnetism, antiferromagnetism has also been observed in condensed matter physics. In an antiferromagnet, one-half of the atomic dipole moments are aligned on one sublattice and the other half are aligned in the opposite direction on the second sublattice. Although there is no net magnetic moment in an antiferromagnet, the state is ordered; i.e., it breaks isotropy like a ferromagnet. In analogy to the spin arrangement in antiferromagnetism, a unique proton-neutron spin coupling giving rise to rotational band structures in nearly spherical nuclei was proposed by Frauendorf [3]. Since then the phenomenon called twin-shears mechanism or more commonly, antimagnetic rotation (AMR), has gained much scientific interest.

The AMR is expected to be observed in the same mass region that is also prone to magnetic rotation [3]. This expectation is found to be true only in one mass region $A \sim 100$–110 so far. A number of magnetic rotation bands observed in this mass region have already been interpreted within the framework of shears mechanism [3–6], wherein the total angular momentum is represented as a vector sum of the angular momentum of individual valence proton ($\pi g_{\frac{9}{2}}$) holes and neutron ($\nu h_{\frac{11}{2}}$) particles. The AMR bands based on the $\pi g_{\frac{9}{2}}^{-2}$ configuration have also been claimed experimentally in $^{105-108,110}$Cd [7–12] and ^{101,104}Pd [13,14] nuclei. The observed AMR spectrum in each of these nuclei supports the following features.

(i) The magnetic dipole ($M1$) transitions are completely absent in the band because the transverse magnetic moments ($\mu_\perp$) of two subsystems (i.e., consisting of neutron plus di-protons) are antialigned and hence cancels each other contribution.
(ii) The antimagnetic rotor is symmetric with respect to a rotation by 180° about the rotating axis, and as a result the energy levels differ in angular momentum by $2\hbar$ and are connected by weak electric quadrupole ($E2$) transitions reflecting a nearly spherical structure of a system. Moreover, this phenomenon is characterized

*shammalik@yahoo.com

by a decrease of the $B(E2)$ values with an increase in spin; this hence ensures the decrease in charge asymmetry with an increase in angular momentum.

(iii) Signature is a good quantum number for such a type of rotating structure. However, one of the signature partner band is found to be missing in the observed spectrum.

Theoretical progress for the description of AMR was initiated first by Frauendorf [3] and later its semiclassical version was developed by Sugawara and coworkers [15]. In these approaches, the high-spin states are generated by the so-called two-shears-like mechanism, i.e., by simultaneous closing of two valance protons (neutrons) toward the neutron (proton) angular-momentum vector. Further, the mean-field approach, based on geometrical arrangement of angular-momentum composition, was also used for understanding the observed features of these rotational bands [3,16,17].

Recently, Zhao and coworkers [18–20] have extended the mean-field approach using covariant density functional formalism for investigating the AMR spectrum. For a complete understanding of the spectrum, they have incorporated the terms like scalar ($\bar{\psi}\psi$), pseudoscalar ($\bar{\psi}\gamma^5\psi$), vector ($\bar{\psi}\gamma^\mu\psi$), pseudovector ($\bar{\psi}\gamma^\mu\gamma^5\psi$), and antisymmetric tensor ($\bar{\psi}\frac{\iota}{2}(\gamma^\mu\gamma^\nu-\gamma^\nu\gamma^\mu)\psi$) in their formalism. They have noticed for the first time a strong contribution of polarization effects on the measured quadrupole moments [i.e., the $B(E2)$ values]. In earlier calculations these effects were either completely absent or were taken into account only partially by minimizing the rotational energy with respect to few deformation parameters. However, the tilted axis cranking plus covariant density functional calculations are not so simple, and therefore an alternative formalism based on the r-helicity state is presented in this paper. This formalism has been proposed on the basis of following experimental observations.

In a more recent experiment on ^{101}Pd nucleus, a reported negative-parity AMR band forms the yrast-line above $I=\frac{11}{2}\hbar$ [13,21]. Note that in this spectrum the electric-dipole ($E1$) transitions prevail from the $\nu h_{\frac{11}{2}}$ band to the $\nu d_{\frac{5}{2}}$ band. This aspect corresponding to the $\nu h_{\frac{11}{2}}$ and $\nu d_{\frac{5}{2}}$ orbitals (i.e., Parity change, $\Delta\Pi=-1$ and $\Delta l=\Delta j=3$) is related to possible octupole correlation in this nucleus. Such octupole correlations are possible only if the weak perturbation H_W violates time-reversal ($\hat{T}$) symmetry along with space-inversion (Π) symmetry [22]. Both these violations lead to a pseudo-Hermitian Hamiltonian, $H_{\Pi T}$, which generates a real discrete spectrum above $I=\frac{11}{2}\hbar$. Zhao and coworkers [18] have incorporated its (pseudocharacter) contribution in their relativistic Lagrangian.

The violation of time-reversal symmetry is also apparent when considering the following. The observed energy levels in the $\nu(h_{\frac{11}{2}})$ band differ in angular momentum $\Delta I=2\hbar$ and are connected by weak electric quadrupole ($E2$) transitions; hence a spheroidal structure with axis of rotation perpendicular to symmetry axis is supported. The signature partners are generally seen for such type of rotating nuclei and the states with opposite signature are related by time-reversal symmetry. However, one of the signature partner bands is completely missing in the observed $\nu(h_{\frac{11}{2}})$ spectrum and as a result time-reversal symmetry gets violated. An individual (i.e., parity and time-reversal) violation is supported by the r helicity (hereafter referred to as *helicity*) formalism. Therefore, its (helicity) introduction in the particle wave function may resolve the paradoxical situation, i.e., how does the AMR band emerge in a given nucleus? This study may open up the possibilities of discovering AMR bands in other mass domains.

In this paper, the concept of helicity has been introduced for the first time in explaining the origin of the AMR spectrum. Throughout the discussion I quote an observed $\nu h_{\frac{11}{2}}$ band in ^{101}Pd whose AMR character has already been established by myself and my coworkers [13] using the framework of a semiclassical rotor model as well as a cranked shell model. A description of the helicity formalism together with appropriate symmetries is given in Sec. II. The results and discussion are given in Sec. III. Our conclusions are summarized in Sec. IV.

II. THE HELICITY FORMALISM

An interaction between particles with spins (i.e., $\pi(g_{\frac{9}{2}})^{-2}$) is usually an operator in the spin space. The present generalization of the helicity formalism projects the spin of proton 1 ($\vec{s}_{\pi_1}$) on the direction of $\vec{r}_1$ and the spin of proton 2 ($\vec{s}_{\pi_2}$) on the direction $\vec{r}_2$ and replaces the operators in spin space by their matrix elements between states of a given helicity. It is worthwhile to mention here that it (helicity) is also the component of total angular momentum ($\vec{j}$) of a particle along the direction of $\vec{r}$, because the orbital angular momentum ($\vec{l}=\vec{r}\times\vec{p}$) is always perpendicular to $\vec{r}$ and, consequently, its projection (m_l) on the axis of quantization, i.e., the $\vec{r}$ axis, is zero. Keeping these points in mind, a complete formalism is presented below.

Bohr and Mottelson [23] have already represented the fermion wave function in helicity bases and pointed out that it is equivalent to the rotational wave function of a system whose intrinsic shape possesses an axial symmetry. Following their footsteps, the bound state of a spin-$\frac{1}{2}$ particle in helicity formalism is carried out. The usual wave function for a spin-$\frac{1}{2}$particle moving in a spherically symmetric and parity conserving potential is given by

$$\mid jm\rangle = f_{lj}(r)\sum_{\mu,\sigma}\langle l\frac{1}{2}\mu\sigma \mid jm\rangle Y_l^\mu(\theta,\phi)\mid\sigma\rangle, \qquad (1)$$

where $\mid\sigma\rangle$ is the spin eigenfunction with a projection σ along the axis of quantization and $f_{lj}(r)$ is a normalized-radial function. The angles θ and ϕ describe the direction of $\vec{r}$ in a fixed reference frame S as shown in Fig. 1. In the helicity representation, the spin orientation refers to a rotated coordinate system S' whose Z' axis is in the direction of unit vector $\hat{e}_r$ (see Fig. 1). The orientation of S' with respect to the fixed frame S is represented by three Euler angles, namely the polar angles θ,ϕ, of $\vec{r}$ and third angle ψ. The Euler angle ψ is fixed by choosing the X' and Y' axes of S' so that S' is obtained from S by a rotation through an angle θ about an axis with the direction of $Z\times Z'$. Therefore, the Euler angles of S' are ϕ,θ, $\psi=-\phi$. The spherical harmonic can be replaced by a matrix element of the rotation operator (D function) which takes the

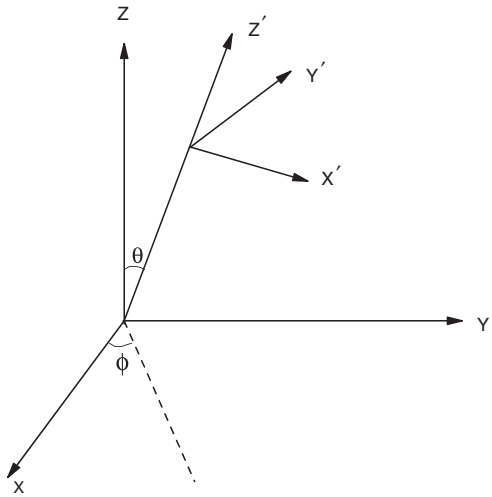

FIG. 1. The fixed frame of reference X, Y, Z and the helicity frame X', Y', Z'.

axis of quantization in the direction of $\vec{r}$, i.e.,

$$Y_l^{\mu}(\theta,\phi) = \sqrt{\frac{2l+1}{4\pi}} D^{l*}_{\mu,0}(\phi,\theta,\psi). \tag{2}$$

The Euler angle ψ is related to some origin; when rotated around $\vec{r}$, the spherical harmonic does not depend on it. Also, $\mid \sigma\rangle$ can be expressed in terms of two helicity functions $\mid h\rangle$ which have a projections $h = \pm\frac{1}{2}$ along $\vec{r}$

$$\mid \sigma\rangle = \sum_h D^{\frac{1}{2}*}_{\sigma,h}(\phi,\theta,\psi) \mid h\rangle. \tag{3}$$

Substituting Eqs. (2) and (3) into Eq. (1) and using the Clebsch-Gordan series for the product of two rotation matrix elements together with their orthonormality constraint, the normalized-state $\mid jm\rangle$ in helicity bases becomes

$$\langle h \mid jm\rangle = \sqrt{\frac{2j+1}{16\pi^2}} f_{lj}(r)\Big[D^{j*}_{m,-\frac{1}{2}}(\phi,\theta,\psi) \mid h = -\frac{1}{2}\rangle + (-1)^{l+j-\frac{1}{2}} D^{j*}_{m,\frac{1}{2}}(\phi,\theta,\psi) \mid h = \frac{1}{2}\rangle\Big]. \tag{4}$$

The wave function (4) of a particle consists of a linear combination of two states which differ in helicity. It does not mean that a particle having positive helicity changes itself into that of negative helicity. This implies that reversed helicity does not occur. Under rotation, it is quite possible that the direction of $\vec{r}$ changes but the helicity of a particle remains unchanged in a system. Thus, the wave function (4) clearly represents the rotational state with definite j and h of a system whose intrinsic shape possesses an axial symmetry. Further, the axial symmetry makes it impossible to distinguish orientations differing only in the value of third Euler angle ψ, and this variable is redundant. Instead of treating the Euler angle ψ as a redundant variable, one may constrain ψ to have a definite value, such as $\psi = 0$ or $\psi = -\phi$.

A. Operation of parity- and time-reversal symmetries on helicity state

The action of parity operator Π on a presently discussed helicity state is exactly same as for standard p helicity [24] because the vector $\vec{r}$ and the impulsion behave similarly. Therefore,

$$\Pi \mid h\rangle = \eta(-)^{s-h} \exp(\imath\pi j_y) \mid -h\rangle, \tag{5}$$

where η is the intrinsic parity of the particle (i.e., $\eta = +1$ for nucleon). The operator $\exp(\imath\pi j_y)$ corresponds to a rotation about y axis through an angle 180°.

The action of the time-reversal operator $\hat{T}$ on a helicity state is accomplished as

$$\hat{T}|h\rangle = (-)^{s+h}|-h\rangle, \tag{6}$$

because $\hat{T}$ does not change the vector $\vec{r}$.

An individual violation of parity- and time-reversal symmetry is noticed in the helicity represented wave function (4) but their (parity and time-reversal) combined operation remains invariant except for the reflection symmetry about a plane. Thus, the helicity representation (4) for the wave function of a particle with spin $\frac{1}{2}$ is equivalent to the representation for rotational wave function of a system whose intrinsic shape possesses an axial symmetry but not the reflection symmetry.

It is quite interesting to notice here that the system represented by wave function (4) possesses an axial symmetric shape in which parity is no longer a good quantum number, i.e., it refers to a pear-shaped system with the z axis as the symmetry axis. For such type of a system, a combination of signature- and parity-quantum numbers is conserved rather than the signature alone. Under this combined symmetry (signature plus parity), the rotational states with even parity having plus (minus) signature get separated from odd-parity with minus (plus) signature. Further, the states with opposite signature are related by time-reversal symmetry, which also gets violated in the present system represented by wave function (4). As a result, one of the signature partner bands disappears from the rotating system. Thus, the violation of reflection symmetry ensures that one of the signature partner bands is missing and, hence, explains the most prominent feature of the observed spectrum.

III. RESULTS AND DISCUSSION

At the bandhead, the angular-momentum vectors $\vec{j}_{\pi_1}$ and $\vec{j}_{\pi_2}$ of two proton holes $[\pi(g_{\frac{9}{2}})^{-2}]$ are pointing opposite to each other and are nearly perpendicular to the neutron $[\nu(h_{\frac{11}{2}})]$ angular momentum $\vec{j}_\nu$. The reference frame is chosen in such a way that the Euler angles ϕ_1, θ_1, $\psi_1 = -\phi_1$ describe a coordinate system with its z axis along $\vec{r}_1$ and $\phi_2, \theta_2, \psi_2 = -\phi_2$ another one with its z axis along $\vec{r}_2$. In order to study the rotational spectra, the axis of quantization is chosen along $\vec{r}_1$ together with a frame of reference for proton 2 given by Euler angles ($\phi_2 = 0$, $\theta_2 = 2\theta$, $\psi_2 = -\phi_2 = 0$), i.e., the vectors $\vec{r}_1$ and $\vec{r}_2$ are oriented at an angle $2\theta(= 180^0)$ as shown in Fig. 2. I mention here that this figure is drawn for the purpose of next subsection and that is why angle between the vectors $\vec{j}_{\pi_1}$ and $\vec{j}_{\pi_2}$ is shown to be 2θ. As a result, two protons in the $g_{\frac{9}{2}}$ orbital lying

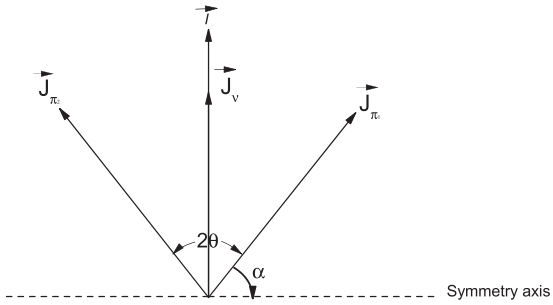

FIG. 2. Pictorial representation of total angular momentum generated by diprotons in which axis of quantization is chosen along particle 1 together with a frame of reference of particle 2 having Euler angles ($\phi_2 = 0, \theta_2 = 2\theta\ \psi_2 = 0$).

at position vectors $\vec{r}_i$ (with $i = 1,2$) follow helical orbits (i.e., left- and right-handed) in a rotating field, whose $+\frac{1}{2}$ spin gives one helicity state, i.e., $|h_1\rangle$ while the $-\frac{1}{2}$ gives another helicity state $|h_2\rangle$. Both these helicity functions $|h\rangle$ have projections $h = \pm\frac{1}{2}$ along the quantization axis $\vec{r}_1$.

One of the major advantages of using the helicity state is that there is no need to separate total angular momentum $\vec{j}$ into orbital and spin parts, because the resultant orbital angular momentum $\vec{L}$ due to diprotons is always perpendicular to the symmetry axis and generates the centrifugal term $\frac{\hbar^2}{2\Im}\vec{L}^2$. Here $\Im$ is the inertia tensor. For the observed negative-parity band, the $\Im$ is estimated from the slope of angular momentum I vs. the rotational frequency $\hbar\omega$ plot and it comes out to be $15.5\,\hbar^2$ MeV^{-1}. The neutron acts as a spectator and contributes to the bandhead angular momentum only. Thus, a complete rotational spectrum is generated by the centrifugal term. The matrix elements $\langle jmh_1{}'h_2{}'|\vec{L}^2|jmh_1h_2\rangle$ of the centrifugal term for a given h_1, h_2 with $h = h_1 - h_2$ are given follows.

Case I: If $h_1{}' = h_1$ and $h_2{}' = h_2$, then

$$\langle jmh_1{}'h_2{}'|\vec{L}^2|jmh_1h_2\rangle = j(j+1) - h^2 + s_{\pi_1}(s_{\pi_1}+1) - h_1{}^2 + s_{\pi_2}(s_{\pi_2}+1) - h_2{}^2. \quad (7)$$

Case II: If $h_1{}' = h_1 \pm 1$ and $h_2{}' = h_2$, then

$$\langle jmh_1{}'h_2{}'|\vec{L}^2|jmh_1h_2\rangle = -\sqrt{j(j+1) - h(h\pm 1)}\sqrt{s_{\pi_1}(s_{\pi_1}+1) - h_1(h_1\pm 1)}. \quad (8)$$

Case III: If $h_1{}' = h_1$ and $h_2{}' = h_2 \pm 1$, then

$$\langle jmh_1{}'h_2{}'|\vec{L}^2|jmh_1h_2\rangle = -\sqrt{j(j+1) - h(h\mp 1)}\sqrt{s_{\pi_2}(s_{\pi_2}+1) - h_2(h_2\pm 1)}. \quad (9)$$

Case IV: If $h_1{}' = h_1 \pm 1$ and $h_2{}' = h_2 \pm 1$, then

$$\langle jmh_1{}'h_2{}'|\vec{L}^2|jmh_1h_2\rangle = \sqrt{s_{\pi_1}(s_{\pi_1}+1) - h_1(h_1\pm 1)}\sqrt{s_{\pi_2}(s_{\pi_2}+1) - h_2(h_2\pm 1)}. \quad (10)$$

The calculated rotational energy E vs. the angular momentum J is shown in Fig. 3 (full line). The observed negative-parity spectrum of ^{101}Pd is also shown as solid circles connected with solid line in this figure. The experimental energy spectrum is reproduced in an excellent way by the present helicity-based calculations. Therefore, we can conclude that both the helical orbits contribute to the observed rotational excitation energy.

Further, the transition probability $B(E2)$ can be obtained within the semiclassical approximation as

$$B(E2) = |\langle j_f m|r^2 Y_{20}|j_i m\rangle|^2 = \frac{5}{4\pi}\left|C^{j_i 2 j_f}_{\frac{1}{2}0\frac{1}{2}}\right|^2 |\int_0^\infty dr f_{l_f j_f}(r) r^4 f_{l_i j_i}|^2. \quad (11)$$

The $B(E2)$ values represented by Eq. (11) generally increase with an increase in angular momentum, whereas the observed spectrum shows a gradual decrease in the reduced transition probability with increase in spin. This decrease in transition probability can be understood from the following discussion. The quadrupole moment operator in $B(E2)$ of the rotational spectrum involves the deformation degrees of freedom for a given configuration. Also, the helicity operator always commutes with rotation. Under rotation, the fermion having positive helicity state $|+h\rangle$ goes one way circular motion around the complex plane, while the fermion with $|-h\rangle$ goes the other way. This implies that the phase of each particle quantum helicity state keeps on changing and hence the degree of polarization also changes (i.e., increases) with a gradual increase in rotation. As a result an ordered (polarized) state emerges at a critical rotational frequency $\hbar\omega$ which breaks down the isotropy symmetry of the system and an AMR band emerges. This change in polarization also rearranges the charge distribution in a rotating system which changes the quadrupole moment and hence the $B(E2)$ values accordingly.

Further, in the present model, the total angular momentum is generated along an axis perpendicular to symmetry axis. For such type of pictures, a gradual increase in rotational frequency generally drives the nucleus toward sphericity and, as result, a gradual decrease in the $B(E2)$ values may occur with increase in angular momentum. It is quite evident from equation (11) that the calculated $B(E2)$ values involve the intrinsic degrees of freedom, which have not been included in the present phenomenological model. Therefore, a complete microscopic development of the helicity based wave function will pinpoint the exact behavior of the $B(E2)$ values and this study is in progress.

A. Relevance with the twin-shears mechanism

Finally, it is quite interesting to notice that the present formalism fully supports the twin-shears mechanism, which is popularly known for these bands. In an antimagnetic rotor, two angular-momentum vector blades $\vec{j}_{\pi_1}$ and $\vec{j}_{\pi_2}$ of the proton

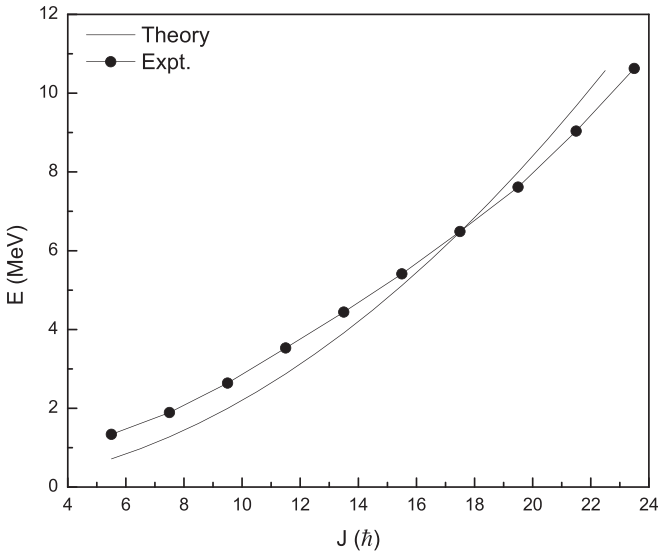

FIG. 3. The calculated rotational energy vs. angular momentum is shown as full line. Also, the solid circles connected with solid line show the observed spectrum of the negative-parity AMR band in the ^{101}Pd nucleus.

holes are stretched apart, each coupled nearly perpendicular to the angular-momentum vector $\vec{j}_\nu$ of a neutron particle, such that the bandhead angular momentum is $\vec{j}_\nu$. This type of configuration is shown in Fig. 2 with angle $2\theta = 180^\circ$ at the bandhead. The high-spin states in a spectrum are generated due to the gradual closing of the proton blades $\vec{j}_{\pi_1}$ and $\vec{j}_{\pi_2}$ towards the neutron angular momentum $\vec{j}_\nu$ with its resultant angular momentum always pointing towards $\vec{j}_\nu$. It is worthwhile to mention here that in the helicity formalism the resultant angular momentum is also obtained along an axis perpendicular to symmetry axis and, hence, it is fully consistent with the twin-shears mechanism.

Further, for an axially symmetric shape, Bohr and Mottelson [22] have already identified the K-quantum number with the helicity value. Here, the quantum number K represents the angular momentum of the intrinsic motion and has a fixed value for the rotational band based on a given intrinsic state. For the $\pi(g_{\frac{9}{2}})^{-2} \otimes \nu(h_{\frac{11}{2}})$ configuration, two symmetric shears each having angle θ are formed. It is quite evident from Fig. 2 that the quantum number K is equal to $j_\pi \sin\theta$ and its resemblance with helicity can easily be drawn as follows. For a particle of mass m, a complete set of orthogonal states are always characterized by position vector $\vec{r}$ and definite $(2j+1)$ helicity $h = -j, -j+1, \ldots, +j$ values.

Also, in the semiclassical picture of the twin-shears mechanism [10,25], the resultant angular momentum is related to shear angle θ between $\vec{j}_\pi$ and $\vec{j}_\nu$ and is given by the expression

$$J = j_\nu + 2j_\pi \cos\theta + \Im\left(\frac{1.5V_{\pi\nu}\cos\theta}{j_\pi} - \frac{6V_{\pi\pi}\cos 2\theta \cos\theta}{n j_\pi}\right). \quad (12)$$

A systematic study of the AMR band infers the interaction strengths $V_{\pi\nu}$ and $V_{\pi\pi}$ equal to 1.2 and 0.15 MeV, respectively. One neutron particle and two proton holes fix $n = 2$ with

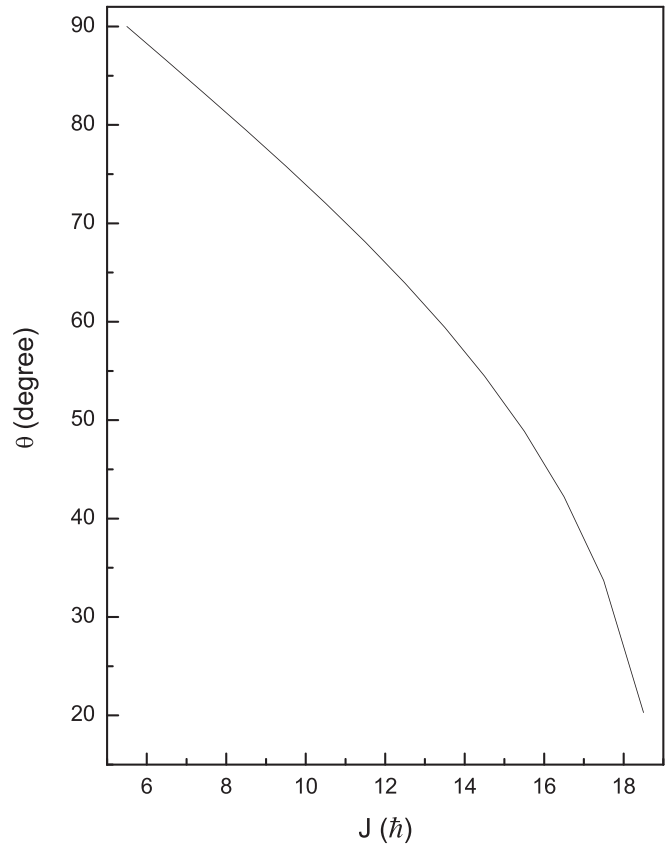

FIG. 4. Variation of shears angle θ vs. the angular momentum.

$j_\nu = 5.5\,\hbar$ and $j_\pi = 4.5\,\hbar$. The inertia parameter has already been estimated to be $15.5\,\hbar^2$ MeV^{-1}.

Equation (12) is a transcendental equation and its numerical solution fixes θ for each angular momentum and is shown in Fig. 4. Its decreasing trend of θ vs. the angular momentum ensures that

$$B(E2) \propto \left|C^{j_i 2 j_f}_{K0K}\right|^2 \propto \sin^4\theta, \quad (13)$$

where $B(E2)$ values decrease with an increase in angular momentum. On the other hand, the total angular momentum is generated along an axis perpendicular to symmetry axis and it involves $\cos\theta$. A decrease in θ increases the angular momentum and hence the rotational energy.

Thus, the experimental spectrum as well as the $B(E2)$ values of the recently observed AMR spectrum in ^{101}Pd are fully consistent with the helical represented states. This simple formalism has completely resolved the paradoxical situation regarding how the AMR emerges in a nucleus. It is worthwhile to mention here that its microscopic version will pinpoint complete features of the AMR spectrum.

B. Role of octupole correlation in the AMR spectrum

As stated above, the octupole correlations likely to play a role in generating the AMR spectrum. This conclusion has been drawn on the basis of the following considerations. Bohr and Mottelson [22] have already pointed out that for configurations with particles in unfilled shells, there may occur

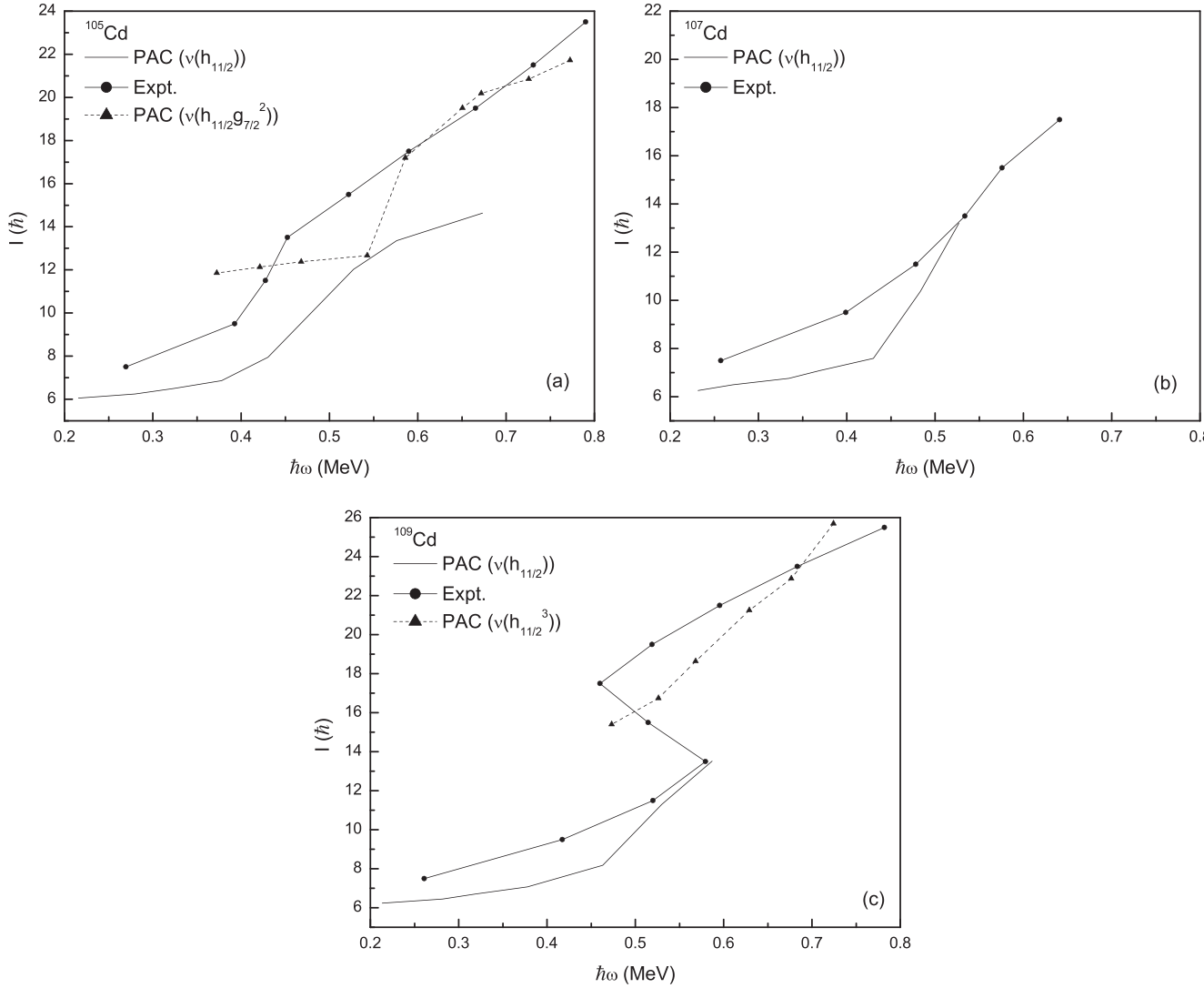

FIG. 5. The experimental and calculated angular momentum I vs. the rotational frequency $\hbar\omega$ for the ^{105,107,109}Cd isotopes.

strong octupole transitions between orbits within a major shell ($1g_{\frac{9}{2}} \longleftrightarrow 2p_{\frac{3}{2}}$ for shells 28–50; $1h_{\frac{11}{2}} \longleftrightarrow 2d_{\frac{5}{2}}$ for shells 50–82; $1i_{\frac{13}{2}} \longleftrightarrow 2f_{\frac{7}{2}}$ for shells 82–126, and $1j_{\frac{15}{2}} \longleftrightarrow 2g_{\frac{9}{2}}$ for shells above 126). This implies that in normally deformed nuclei, the tendency towards octupole correlation occurs just above a closed shell with particle numbers (i.e., N or Z) ∼34 ($1g_{\frac{9}{2}} \longleftrightarrow 2p_{\frac{3}{2}}$ coupling), ∼56 ($1h_{\frac{11}{2}} \longleftrightarrow 2d_{\frac{5}{2}}$ coupling), ∼88 ($1i_{\frac{13}{2}} \longleftrightarrow 2f_{\frac{3}{2}}$ coupling), and ∼134 ($1j_{\frac{15}{2}} \longleftrightarrow 2g_{\frac{9}{2}}$ coupling). The AMR bands have already been confirmed in ^{100}Pd [26] and ^{101}Pd [13,17]. The octupole transitions have clearly been observed in these nuclei which (^{100}Pd and ^{101}Pd) fall in the $N \sim 56$ region. The Cadmium-isotopes, which also belong to that region, have been described as the optimal candidates for the observed antimagnetic rotation and their low-lying levels have already been interpreted as quadrupole-octupole oscillations [27]. Therefore, the role of octupole correlation in the AMR spectrum is discussed with reference to odd-A i.e., ^{105,107,109}Cd isotopes.

In odd-A nuclei, the $E1$ and $E3$ (i.e., the dipole and octupole) transitions between opposite-parity states are considered to be the manifestation of collective and intrinsic degrees of freedom ensuing from the presence of quadrupole-octupole shape deformations [28]. At low angular momenta, the nucleus is characterized by a soft-octupole shape superposed on the top of a stable quadrupole deformation, while with an increasing angular momentum the resultant quadrupole-octupole shape is stabilized. Then it is considered that at low angular momentum the system is capable of performing octupole oscillations. At higher angular momenta, the octupole deformation gets stabilized and the nucleus performs a rotation that is completely governed by the complex quadrupole deformation. Keeping these points in mind, a systematic analysis of each of the odd-A i.e., ^{105,107,109}Cd isotopes, is carried out.

The $J^{\Pi} = \frac{11}{2}^{-}$ level appears in all the three odd-A Cd isotopes [29]. It is noticed that the energy gap between the $\frac{11}{2}^{-}$ state and the ground sate $J^{\Pi} = \frac{5}{2}^{+}$ in ^{105,107}Cd is larger than that of ^{109}Cd. This large energy gap provides a considerable space to several single particle states and as a result the collective nature appears in the ^{105,107}Cd-isotopes. Kisyov and

TABLE I. The PAC model parameters are calculated for the ground-state and band-crossing negative-parity configurations in ^{105,109}Cd isotopes. These parameters for the ^{107}Cd isotope for ground-state negative-parity configuration are also listed.

Isotope	Configuration	Δ_p (MeV)	Δ_n (MeV)	ϵ_2	ϵ_4	γ
^{105}Cd	$\pi\left[\left(g_{\frac{9}{2}}\right)^{-2}\right]_0 \otimes \nu\left(h_{\frac{11}{2}}\right)$	1.1578	1.0756	0.123	−0.008	15.2°
^{105}Cd	$\pi\left[\left(g_{\frac{9}{2}}\right)^{-2}\right]_0 \otimes \nu\left(h_{\frac{11}{2}} g^2_{\frac{7}{2}}\right)$	1.1578	1.0756	0.162	0.0	4.6°
^{107}Cd	$\pi\left[\left(g_{\frac{9}{2}}\right)^{-2}\right]_0 \otimes \nu\left(h_{\frac{11}{2}}\right)$	1.1548	1.0759	0.139	0.01	10.3°
^{109}Cd	$\pi\left[\left(g_{\frac{9}{2}}\right)^{-2}\right]_0 \otimes \nu\left(h_{\frac{11}{2}}\right)$	1.1698	1.1136	0.137	0.009	9.6°
^{109}Cd	$\pi\left[\left(g_{\frac{9}{2}}\right)^{-2}\right]_0 \otimes \nu\left(h^3_{\frac{11}{2}}\right)$	1.1698	1.1136	0.157	0.01	4.5°

coworkers [30] have ensured experimentally that (^{105,107}Cd) $\frac{11}{2}^-$-level decays via a dominant $E1$ branch, whereas ^{109}Cd isotope decays via an $M2$ transition. Further, the $E1$-decay mode (i.e., $\frac{31}{2}^- \rightarrow \frac{29}{2}^+$ with $E_\gamma = 803$ keV) just after the band crossing has also been observed in the ^{109}Cd isotope [16]. However, a large number of $E1$ transitions could not be observed in these isotopes. A sudden drop of intensity of the populated states at high angular momentum I could be responsible for the missing $E1$ transitions. Thus, the lowest excited negative-parity band consisting of $\Delta I = 2$ transitions in each of the odd-A cadmium isotope is controlled by a soft-octupole shape superposed on the top of a stable quadrupole deformation. Macroscopic-microscopic models [31,32] have already predicted that the octupole deformation of the ground state does not persist to high-angular-momentum I. Smith and coworkers [33] have also pointed out that a sudden drop in intensity of $E1$ at high angular momentum is the fingerprint of such a change in shape.

I have tried to understand the absence of octupole contribution at higher angular momentum along the band using the principal axis cranking (PAC) model. The PAC calculations based on the Nilsson approach are carried out for each odd-A cadmium isotope. Considering the bandhead angular momenta, parity, and excitation energy, the configuration $\pi[(g_{\frac{9}{2}})^{-2}]_0 \otimes \nu(h_{\frac{11}{2}})$ has been chosen for each cadmium isotope. In this configuration, $\pi[(g_{\frac{9}{2}})^{-2}]_0$ represents paired quasiparticles and contributes zero angular momentum. In all these cases, the proton and neutron pairing parameters (Δ_p and Δ_n) are chosen as 80% of the odd-even mass difference. The deformation parameters ($\epsilon_2, \epsilon_4, \gamma$) are determined self-consistently by a minimization of the total energy. The values of calculated Δ_p, Δ_n, and the corresponding deformation parameters ϵ_2, ϵ_4, and γ for each of the three cadmium isotopes are given in Table I.

Figures 5(a)–5(c) show the calculated as well as the experimental data of angular momentum I vs. the rotational frequency $\hbar\omega$ for the three Cd isotopes. I shall first analyze the case of the ^{105}Cd isotope [refer to Fig. 5(a)] in detail and then discuss the results for other isotopes. The observed yrast band built on the $\nu(h_{\frac{11}{2}})$ bandhead configuration is reasonably close to the one predicted by the PAC model. The basic configuration for this band is expected to be the prolate-driving $\nu(h_{\frac{11}{2}})$ orbital. However, the difference between the observed and calculated values may arise due to octupole oscillations which this system generally performs at low angular momentum. Further, the observed spectrum shows band crossing around the rotational frequency ∼0.4 MeV. The PAC model calculations predict the band crossing resulting from the alignment of the $\nu(g_{7/2})^2$ pair. Thus, after the band crossing, the high-spin states above $\frac{27}{2}\hbar$ are generated due to alignment of a pair of $\pi(g_{\frac{9}{2}})^{-2}$ proton holes with the configuration $\pi[(g_{\frac{9}{2}})^{-2}] \otimes \nu(h_{\frac{11}{2}} g^2_{7/2})$ along with the parameters listed in Table I. It is quite obvious from the listed parameters that a prolate shape emerges after the band crossing and reproduces the observed angular momentum vs. the rotational frequency plot. Thus, a comparison with observed data reveals that at low angular momenta the system is capable of performing octupole oscillations. At higher angular momenta, the octupole deformation gets stabilized and the nucleus performs a rotation that is completely governed by the complex quadrupole deformation.

Kisyov and coworkers [30] have already confirmed that the structure of ^{107}Cd is quite similar to that of ^{105}Cd. Unfortunately, its spectrum after band crossing has yet not been reported. Again, its observed yrast band built on a $\nu(h_{\frac{11}{2}})$ bandhead configuration is reasonably close to the predicted one by the PAC model [Fig. 5(b)]. The differences between the observed and calculated values reveal that at low angular momenta the system is capable of performing octupole oscillations, and these oscillations decrease with the increase in angular momentum and hence ensure the prolate shape just near the band-crossing frequency.

In Fig. 5(c), the results of ^{109}Cd along with experimental data are shown. The observed back-bending above $\frac{31}{2}\hbar$ is explained with the configuration $\pi[(g_{\frac{9}{2}})^{-2}] \otimes \nu(h^3_{\frac{11}{2}})$ along with the parameters listed in Table I. Again its comparison with observed data supports similar conclusions as drawn in case of ^{105}Cd and ^{107}Cd isotopes.

Further, the experimental and calculated $B(E2)$ values for ^{105}Cd and ^{109}Cd isotopes in the high-spin range are compared in Figs. 6(a) and 6(b), respectively. Except for their decreasing trends, the calculated values are of same order of magnitude as that of the observed ones. It is worthwhile to mention here that the decrease of $B(E2)$ values with an increase in angular momentum is a clear signature of the shearslike mechanism.

These results ensure that the octupole deformation gets stabilized at higher angular momentum and the nucleus performs an AMR rotation that is completely governed by the complex quadrupole deformation. Bohr and Mottelson [22] have pointed out that the low-frequency quadrupole-octupole oscillations contribute isoscalar and isovector polarization to a

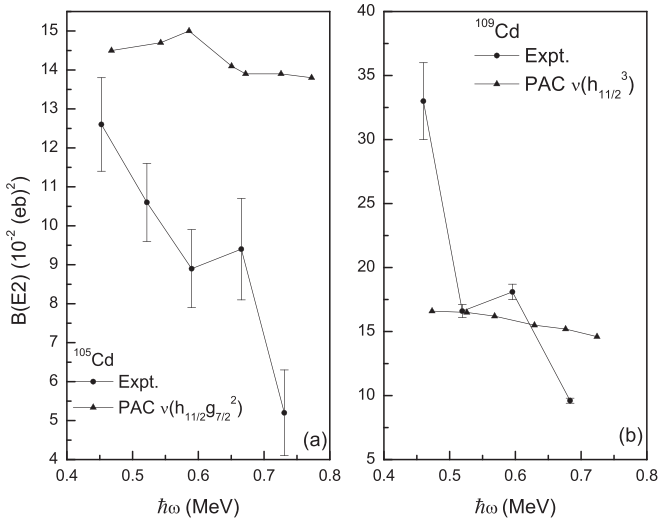

FIG. 6. The experimental and calculated $B(E2)$ values vs. $\hbar\omega$ for the ^{105,109}Cd isotopes.

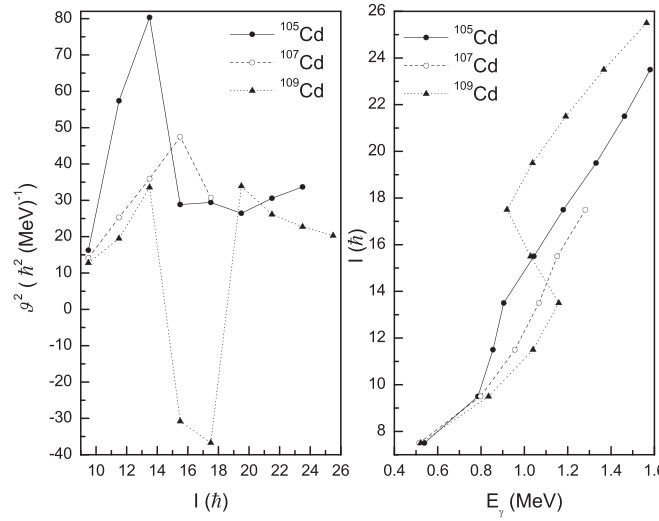

FIG. 7. Left panel shows the observed dynamic moment of inertia $\Im^2$ vs. the angular momentum I, whereas the right panel shows the variation of angular momentum I vs. the γ-ray energy E_γ.

system and these polarizations have been included by Zhao and coworkers [18,19] in their covariant density functional formalism for explaining the AMR spectrum. These points reveal that the octupole mode may play some contribution in fixing the antimagnetic character in a system, i.e., why it is one of the rare phenomena that has been observed by using sophisticated detectors.

C. Symmetries responsible for AMR spectrum

Zhao and coworkers [18,19] have noted that the combined operation of space reflection (Π), time-reversal (T), and the reflection in the y direction remains invariant, i.e., $[H, \Pi_y T] = 0$, and is aids in explaining the AMR spectrum. Therefore, it is important to understand the role of each of these individual symmetries in the case of a deformed nucleus with an axis of symmetry as the z axis. Such an axial-symmetric shape in which parity alone is no longer a good quantum number generally refers to a pear-shaped structure. Then the combined operation of both parity and reflection in the y direction (i.e., Π_y) is good symmetry instead of reflection in the y direction alone. Under this combined symmetry operation, the rotational states with even parity having plus (minus) signature get separated from odd parity with minus (plus) signature. Since $[H, \Pi_y T] = 0$ it implies that either both Π_y and time reversal (T) are conserved or violated separately. The latter choice is likely to be more favorable because the signature partner bands with opposite parity have not been observed in the AMR spectrum. Therefore, this combined operation of three symmetries does not support two signature-partner bands with same parity. The present formalism (as discussed in Sec. II A) also ensures similar combined operation of three symmetry operators and, hence, is fully consistent with that of Zhao and coworkers [18,19].

It is worthwhile to mention here that the structure of the ^{107}Cd isotope is quite similar to that of ^{105}Cd as noted by Kisyov and coworkers [30]. A similar point has also been drawn by Roy and Chattopadhyay [25] by plotting the aligned angular momenta i of ^{105,107}Cd isotopes vs. the rotational frequency $\hbar\omega$. It is apparent from their plot (Fig. 2 of Ref. [25]) that the alignment gain ($i \sim 4$) is similar in both of these isotopes. This implies that the neutron-aligned yrast configuration for ^{107}Cd is also similar to that of ^{105}Cd [i.e., $\pi[(g_{\frac{9}{2}})^{-2}]_0 \otimes \nu(h_{\frac{11}{2}} g^2_{7/2})$]. Further, the structural similarity in odd-A $^{105-109}$Cd isotopes can also be understood from the plots shown in Fig. 7. The left panel of Fig. 7 shows the observed dynamic moment of inertia $\Im^2$ vs. the angular momentum I of the negative-parity bands based on the $\nu(h_{\frac{11}{2}})$ bandhead configuration. A nearly similar behavior of $\Im^2$ in both the ^{105,107}Cd isotopes supports above conclusions. Also, a comparison among three odd-A isotopes reveals that collectivity persists up to an angular momentum $\frac{27}{2}\hbar$ and then decreases gradually for higher angular momenta where the excited band configurations start to dominate, leading the nucleus towards noncollective shapes. These noncollective shapes are likely to generate antimagnetic rotation in a system. The angular momentum I vs. the γ-ray energy E_γ plot shown in the right panel of Fig. 7 also favors the same results. However, the negative-parity yrast sequence of the ^{107}Cd nucleus is known only up to $\frac{31}{2}\hbar$ [34], which needs to be extended in order to investigate the possibility of AMR in ^{107}Cd.

IV. CONCLUSIONS

To summarize, we have carried out r-helicity-based analysis of the observed negative parity AMR band in the ^{101}Pd nucleus. The helical modes are found to aid in explaining the observed octupole correlations which force the system to generate an antimagnetic spectrum. The helicity-based wave function supports a pear-shaped structure of a nucleus having an axis of symmetry. This structure conserves a combined operation of parity and signature quantum numbers instead of signature alone. Simultaneous violation of time-reversal symmetry in the helicity-based formalism leads to disappearance of one

of the signature partner band and hence explains one of the prominent observed feature in AMR spectrum. Also, it has been noticed that the degree of polarization breaks down the isotropy symmetry of the nucleus and hence generates an antimagnetic structure. This formalism has been tested successfully for the recently observed negative parity $\Delta I = 2$ antimagnetic spectrum in odd-A ^{101}Pd nucleus. These results establish the importance of helical orbits in the observed AMR spectrum.

ACKNOWLEDGMENT

S.S.M. is thankful to T.I.F.R. Mumbai, India, for providing fruitful discussion.

[1] S. Frauendorf, Nucl. Phys. A **557**, 259 (1993).
[2] G. Baldsiefen *et al.*, Nucl. Phys. A **574**, 521 (1994).
[3] S. Frauendorf, Rev. Mod. Phys. **73**, 463 (2001).
[4] R. M. Clark, S. J. Asztalos, B. Busse, C. J. Chiara, M. Cromaz, M. A. Deleplanque, R. M. Diamond, P. Fallon, D. B. Fossan, D. G. Jenkins, S. Juutinen, N. Kelsall, R. Krücken, G. J. Lane, I. Y. Lee, A. O. Macchiavelli, R. W. MacLeod, G. Schmid, J. M. Sears, J. F. Smith, F. S. Stephens, K. Vetter, R. Wadsworth, and S. Frauendorf, Phys. Rev. Lett. **82**, 3220 (1999).
[5] R. M. Clark and A. O. Macchiavelli, Nucl. Phys. A **682**, 415 (2001).
[6] A. J. Simons, R. Wadsworth, D. G. Jenkins, R. M. Clark, M. Cromaz, M. A. Deleplanque, R. M. Diamond, P. Fallon, G. J. Lane, I. Y. Lee, A. O. Macchiavelli, F. S. Stephens, C. E. Svensson, K. Vetter, D. Ward, and S. Frauendorf, Phys. Rev. Lett. **91**, 162501 (2003).
[7] D. Choudhury, A. K. Jain, M. Patial, N. Gupta, P. Arumugam, A. Dhal, R. K. Sinha, L. Chaturvedi, P. K. Joshi, T. Trivedi, R. Palit, S. Kumar, R. Garg, S. Mandal, D. Negi, G. Mohanto, S. Muralithar, R. P. Singh, N. Madhavan, R. K. Bhowmik, and S. C. Pancholi, Phys. Rev. C **82**, 061308(R) (2010).
[8] S. Roy and S. Chattopadhyay, Phys. Rev. C **87**, 059801 (2013).
[9] A. J. Simons, R. Wadsworth, D. G. Jenkins, R. M. Clark, M. Cromaz, M. A. Deleplanque, R. M. Diamond, P. Fallon, G. J. Lane, I. Y. Lee, A. O. Macchiavelli, F. S. Stephens, C. E. Svensson, K. Vetter, D. Ward, S. Frauendorf, and Y. Gu, Phys. Rev. C **72**, 024318 (2005).
[10] S. Roy *et al.*, Phys. Lett. B **694**, 322 (2011).
[11] D. Choudhury, A. K. Jain, G. A. Kumar, S. Kumar, S. Singh, P. Singh, M. Sainath, T. Trivedi, J. Sethi, S. Saha, S. K. Jadav, B. S. Naidu, R. Palit, H. C. Jain, L. Chaturvedi, and S. C. Pancholi, Phys. Rev. C **87**, 034304 (2013).
[12] P. Datta, S. Chattopadhyay, S. Bhattacharya, T. K. Ghosh, A. Goswami, S. Pal, M. Saha Sarkar, H. C. Jain, P. K. Joshi, R. K. Bhowmik, R. Kumar, N. Madhaban, S. Muralithar, P. V. Rao, and R. P. Singh, Phys. Rev. C **71**, 041305(R) (2005).
[13] V. Singh, S. Sihotra, S. Roy, M. Kaur, S. Saha, J. Sethi, R. Palit, N. Singh, S. S. Malik, H. C. Jain, and D. Mehta, J. Phys. G: Nucl. Part. Phys. **44**, 075105 (2017).
[14] N. Rather, S. Roy, P. Datta, S. Chattopadhyay, A. Goswami, S. Nag, R. Palit, S. Pal, S. Saha, J. Sethi, T. Trivedi, and H. C. Jain, Phys. Rev. C **89**, 061303(R) (2014).
[15] M. Sugawara, Y. Toh, M. Oshima, M. Koizumi, A. Osa, A. Kimura, Y. Hatsukawa, J. Goto, H. Kusakari, T. Morikawa, Y. H. Zhang, X. H. Zhou, Y. X. Guo, and M. L. Liu, Phys. Rev. C **79**, 064321 (2009).
[16] C. J. Chiara, S. J. Asztalos, B. Busse, R. M. Clark, M. Cromaz, M. A. Deleplanque, R. M. Diamond, P. Fallon, D. B. Fossan, D. G. Jenkins, S. Juutinen, N. S. Kelsall, R. Krücken, G. J. Lane, I. Y. Lee, A. O. Macchiavelli, R. W. MacLeod, G. Schmid, J. M. Sears, J. F. Smith, F. S. Stephens, K. Vetter, R. Wadsworth, and S. Frauendorf, Phys. Rev. C **61**, 034318 (2000).
[17] Zhen-Hua Zhang, Phys. Rev. C **94**, 034305 (2016).
[18] P. W. Zhao, J. Peng, H. Z. Liang, P. Ring, and J. Meng, Phys. Rev. Lett. **107**, 122501 (2011).
[19] P. W. Zhao, J. Peng, H. Z. Liang, P. Ring, and J. Meng, Phys. Rev. C **85**, 054310 (2012).
[20] J. Meng, J. Peng, S. Q. Zhang, and P. W. Zhao, Front. Phys. **8**, 55 (2013).
[21] M. Sugawara, T. Hayakawa, M. Oshima, Y. Toh, A. Osa, M. Matsuda, T. Shizuma, Y. Hatsukawa, H. Kusakari, T. Morikawa, Z. G. Gan, and T. Czosnyka, Phys. Rev. C **92**, 024309 (2015).
[22] A. Bohr and B. R. Mottelson, *Nuclear Structure*, Vol. II (Benjamin, New York, 1975).
[23] A. Bohr and B. R. Mottelson, *Nuclear Structure*, Vol. I (Benjamin, New York, 1975).
[24] M. Jacob and G. C. Wick, Ann. Phys. **7**, 404 (1959).
[25] S. Roy and S. Chattopadhyay, Phys. Rev. C **83**, 024305 (2011).
[26] S. Zhu, U. Garg, A. V. Afanasjev, S. Frauendorf, B. Kharraja, S. S. Ghugre, S. N. Chintalapudi, R. V. F. Janssens, M. P. Carpenter, F. G. Kondev, and T. Lauritsen, Phys. Rev. C **64**, 041302(R) (2001).
[27] P. E. Garrett and J. L. Wood, J. Phys. G: Nucl. Part. Phys. **37**, 064028 (2010).
[28] P. A. Butler and W. Nazarewicz, Rev. Mod. Phys. **68**, 349 (1996).
[29] NNDC data base, http://www.nndc.bnl.gov/ensdf.
[30] S. Kisyov, S. Lalkovski, N. Mărginean, D. Bucurescu, L. Atanasova, D. L. Balabanski, Gh. Căta-Danil, I. Căta-Danil, J.-M. Daugas, D. Deleanu, P. Detistov, D. Filipescu, G. Georgiev, D. Ghiţă, T. Glodariu, J. Jolie, D. S. Judson, R. Lozeva, R. Mărginean, C. Mihai, A. Negret, S. Pascu, D. Radulov, J.-M. Régis, M. Rudigier, T. Sava, L. Stroe, G. Suliman, N. V. Zamfir, K. O. Zell, and M. Zhekova, Phys. Rev. C **84**, 014324 (2011).
[31] W. Nazarewicz, P. Olanders, I. Ragnarsson, J. Dudek, and G. A. Leander, Phys. Rev. Lett. **52**, 1272 (1984).
[32] W. Nazarewicz, G. A. Leander, and J. Dudek, Nucl. Phys. A **467**, 437 (1987).
[33] J. F. Smith, J.F.C. Cocks, N. Schulz, M. Aïche, M. Bentaleb, P. A. Butler, F. Hannachi, G. D. Jones, P. M. Jones, R. Julin, S. Juutinen, R. Kulessa, E. Lubkiewicz, A. Płochocki, F. Riess, E. Ruchowska, A. Savelius, J. C. Sens, J. Simpson, and E. Wolf, Phys. Rev. Lett. **75**, 1050 (1995).
[34] D. Jerrestam *et al.*, Nucl. Phys. A **545**, 835 (1992).